Energy Advances

ROYAL SOCIETY OF CHEMISTRY

PAPER

View Article Online
View Journal

Cite this: DOI: 10.1039/d5ya00355e

Study of composite polymer electrolytes incorporating LLZO particles in a PEO matrix in high voltage all solid-state lithium batteries

Sneha Subhas Malunavar,[a] Susan Montes,[a] Sandra Martinez-Crespiera,[b] Gerard Pérez-Pi,[b] Sonja Tischler,[a] Stefano Passerini[a] and Meisam Hasanpoor *[a]

Received 5th December 2025,
Accepted 14th March 2026

DOI: 10.1039/d5ya00355e

rsc.li/energy-advances

The impact of different $Li_7La_3Zr_2O_{12}$ (LLZO) fillers irrespective of dopants on the electrochemical performance of solid polymer electrolytes (SPEs) is systematically investigated. LLZO particles doped with Al and Ta/Nb were synthesized *via* electrospinning (Al-LLZO) and the solid-state reaction (bulk Al-LLZO and Ta/Nb-LLZO), alongside a commercial LLZO Ref. Three SPE composites S1 (electrospun Al-LLZO), S2 (bulk Al-LLZO), and S3 (Ta/Nb-LLZO) were fabricated by dispersing the fillers into a PEO–LiTFSI matrix. Among them, S2 exhibited the highest ionic conductivity (10^{-3} S cm^{-1} at 60 °C), outperforming S1 and S3 (10^{-4} S cm^{-1}). All SPEs demonstrated a stable electrochemical window of 2.5–4.2 V, confirmed *via* cyclic voltammetry. Symmetric cell testing revealed that the Ref sample, with smaller and more uniformly distributed LLZO particles, achieved the lowest overpotential. Full-cell cycling with an NMC811‖SPE‖Li–metal at 60 °C yielded discharge capacities of 80–115 mAh g^{-1} for S2, S3, and the Ref, whereas S1 underperformed. Despite these variations, the solid polymer electrolytes demonstrate promising stability when in contact with both the Li metal anode and the NMC811 cathode, highlighting its potential for use in high voltage solid-state batteries at elevated temperatures.

Introduction

The rapid expansion of the electric vehicle (EV) industry has significantly increased the demand for lithium battery technology over the past decade.[1] Practical applications such as in EVs, robotics, and drones require high performance lithium batteries that meet key criteria, including cost effectiveness, energy density, safety, and cycle life. Specifically, these batteries must achieve an energy density greater than 1000 Wh L^{-1} and a specific energy above 500 Wh kg^{-1}, making it crucial to advance existing lithium technologies to meet these demands.[2]

Currently, commercial lithium batteries use non-aqueous, organic solvent-based electrolytes, which are highly flammable and unstable during cell cycling and pose risks during high temperature operation particularly due to dendrite formation when the lithium metal is used as the anode. SPEs present a promising alternative to address these issues. SPEs offer improved safety and thermal stability compared to their liquid counterparts.[3] They are typically developed by dissolving lithium salts within a polymer matrix. So far, the most extensively studied polymers include polyethylene oxide (PEO), polymethyl methacrylate (PMMA), and polypropylene oxide. These materials generally exhibit a low transference number for alkali ions (such as Li^+), which interact with the polymer matrix, with the anion typically serving as the primary charge carrier. This presents a challenge for their use in devices due to polarization effects. Among these, PEO-based solid SPEs are the most widely researched because some of them form stable complexes with salts and offer high ionic conductivity compared to other polymer hosts. PEO is known to form stable complexes with various lithium salts, including lithium tetrafluoroborate ($LiBF_4$), lithium iodide (LiI), lithium perchlorate ($LiClO_4$), lithium bromide (LiBr), lithium chloride (LiCl), lithium hexafluoroarsenate ($LiAsF_6$), and lithium bis(trifluoromethanesulfonyl)imide (LiTFSI). Among these, the PEO–LiTFSI and PEO–$LiClO_4$ systems are the most extensively investigated.[4–8]

Research indicates that the conduction of Li^+ ions in polymer electrolytes is linked to the local segmental motion of polymer chains, which is more favourable in the amorphous phase of the polymer electrolyte than in the crystalline phase.[9] Therefore, enhancing the SPE material to predominantly feature amorphous regions is crucial for achieving high ionic conductivity at room temperature.

Various methods to improve ionic conductivity in SPEs include incorporating one or more salts into the polymer matrix,[10,11] modifying the polymer host,[12,13] and treating the

[a] Austrian Institute of Technology (AIT) GmbH, Vienna-1210, Austria.
E-mail: sneha.malunavar@ait.ac.at, meisam.hasanpoor@ait.ac.at
[b] LEITAT Technological Centre, Barcelona-08005, Spain

SPEs by exposing them to X-rays, ultraviolet rays, electrons, ion beams, *etc.*[14] Other approaches involve using blended polymer electrolytes,[15] plasticizers,[16] and inorganic fillers.[17,18] These latter can be classified into two categories: active fillers, such as lithium lanthanum zirconate ($Li_7La_3Zr_2O_{12}$, LLZO) and $Li_{0.33}La_{0.557}TiO_3$ (LLTO), and inert fillers, such as SiO_2, Mo_2C, and Al_2O_3.

According to the literature, major challenges hindering the commercialization of solid-state batteries (SSBs) are formation of lithium dendrites and the volume changes that occur during charging and discharging, the unstable interface specifically with high voltage cathodes, and mechanical integrity of the polymer cells. The strong mechanical properties of garnet materials can effectively improve the mechanical integrity; consequently, the mechanical stability of garnet materials is a critical factor in evaluating their suitability as solid electrolytes. However, challenges related to interfacial stability remain under investigation. One promising approach to address this issue involves the incorporation of doped inorganic fillers, which can potentially improve both interfacial compatibility and overall electrochemical performance.[19,20]

Recently, the cubic garnet type inorganic solid electrolyte $Li_7La_3Zr_2O_{12}$ (LLZO) has gained significant interest due to its chemical stability with the lithium metal, wide electrochemical window (>5 V *vs.* Li/Li^+), and high ionic conductivity ($>10^{-4}$ S cm^{-1} at 25 °C).[21,22] Numerous studies have explored the influence of ceramic rich composites in polymer matrices. In one study, Choi *et al.*[23] examined various concentrations of the tetragonal phase LLZO (0, 42.5, 52.5, 62.5, 72.5, and 82.5 wt%) in a PEO matrix. They observed the highest ionic conductivity at 60 °C ($\sim 10^{-3}$ S cm^{-1}) in 52.5 wt% LLZO in the polymer composite. In another study, Cai *et al.*[24] reported a composite electrolyte based on a 3D LLZO framework, which exhibited a Li^+ transference number of 0.61 and an ionic conductivity of 10^{-4} S cm^{-1} at room temperature.

To enhance stability and ionic conductivity, researchers have also explored the doping effects in LLZO particles. A few examples of dopants used in LLZO include aluminium (Al^{3+}), gallium (Ga^{3+}), niobium (Nb^{5+}), and tantalum (Ta^{5+}) among others. Kim *et al.*[25] studied the effect of Al doped LLZO in a PEO–$LiClO_4$ polymer matrix and achieved an ionic conductivity of 10^{-3} S cm^{-1} at 70 °C. Chen *et al.*[26] reported Al doped LLZO incorporated into a PEO polymer matrix. The resulting SPE exhibited an ionic conductivity of 6.19×10^{-4} S cm^{-1} and an electrochemical voltage window of 5.6 V at 60 °C. An all-solid-state lithium battery with the configuration LFP‖SPE‖Li–metal delivered a specific capacity of 143 mAh g^{-1} over 115 cycles at 0.5C. In another study, Ahn *et al.*[27] investigated Al^{3+} and Nb^{5+} co-doped LLZO (referred to as NAL), synthesized *via* the Pechini sol–gel method. This doped LLZO was incorporated into a PEO polymer matrix with succinonitrile (SN). The final electrolyte composition, PEO/LiTFSI–SN–NAL (PLS–NAL), exhibited an ionic conductivity of 3.09×10^{-4} S cm^{-1} at room temperature. The LFP‖PLS–NAL‖Li–metal battery delivered a specific capacity of 152.3 mAh g^{-1} at 45 °C and 129.9 mAh g^{-1} at room temperature. Reis *et al.*[28] developed a PEO-based composite polymer electrolyte using Nb-doped LLZO, and this electrolyte achieved an ionic conductivity of 10^{-4} S cm^{-1} at 60 °C and delivered a specific capacity of 185 mAh g^{-1} for C/20 at 60 °C and a capacity retention of 68% after 50 cycles at C/5 with the NMC811 cathode.

In this work, LLZO particles doped with Al and Ta/Nb were synthesized using two different routes. Al-doped LLZO (S1) was prepared *via* electrospinning, while bulk Al-LLZO (S2) and bulk Ta/Nb-LLZO (S3) were obtained through a conventional solid-state reaction, allowing us to directly compare the influence of the synthesis method on the resulting LLZO filler properties such as the morphology, surface defects and their influence on the cycling performance. Solid polymer electrolytes (SPEs) were subsequently fabricated by incorporating S1, S2, S3, and a commercial LLZO reference powder (LLZO-1920M, denoted as Ref) into a PEO–LiTFSI matrix. For clarity, the resulting SPE composites are referred to as Ref, S1, S2, and S3 throughout the manuscript. The electrochemical performance of these materials was then evaluated in combination with a high-voltage cathode, NMC811. As the aim of this study is to evaluate how LLZO fillers with different synthesis histories and surface chemistries interact with the PEO LiTFSI polymer matrix, rather than to compare specific dopant strategies, these materials provide a representative basis for assessing filler polymer interfacial behaviour in composite solid polymer electrolytes.

Experimental procedures

LLZO synthesis

Solid state synthesis route. The LLZO samples were synthesized using the solid-state reaction method as shown in Fig. 1(a). La_2O_3 and ZrO_2 were used as precursors in stoichiometric ratios, but a 10–15% excess of the lithium precursor was used to compensate for lithium losses during synthesis. Various stoichiometric amounts of dopant precursors (Al_2O_3, Nb_2O_5, or Ta_2O_5) were also incorporated. The solid precursors were mixed and refined using ball milling in isopropanol for 10 hours and then dried at 100 °C for 24 hours. The resulting powder was calcined in air at 900 °C for 8 hours, followed by ball milling for reduction of particle size. The ball milling speed was between 10,000 rpm and 12,000 rpm. A second calcination was subsequently applied to the homogenized powder under the same conditions as the first. The final material was ball milled again and processed to adjust the particle size distribution to meet application requirements.

Synthesis of LLZO by electrospinning. Electrospun Al-LLZO have been synthesized by an electrospinning process followed by a thermal treatment. First a polymeric solution was perpared, as shown in Fig. 1(b). This solution was formulated by mixing the precursor salts (*i.e.*, Li, La, Al and Zr) with PVP in DMF and acetic acid. To optimize the polymeric solution, 20 wt% excess Li was used, and a suitable ratio between the precursor salts and the polymer (1 : 1.6) was selected. For the electrospinning process (Fluidnatek, LE-500), the conditions used were a flow rate of 9 ml h^{-1}, voltages of +25–27 kV

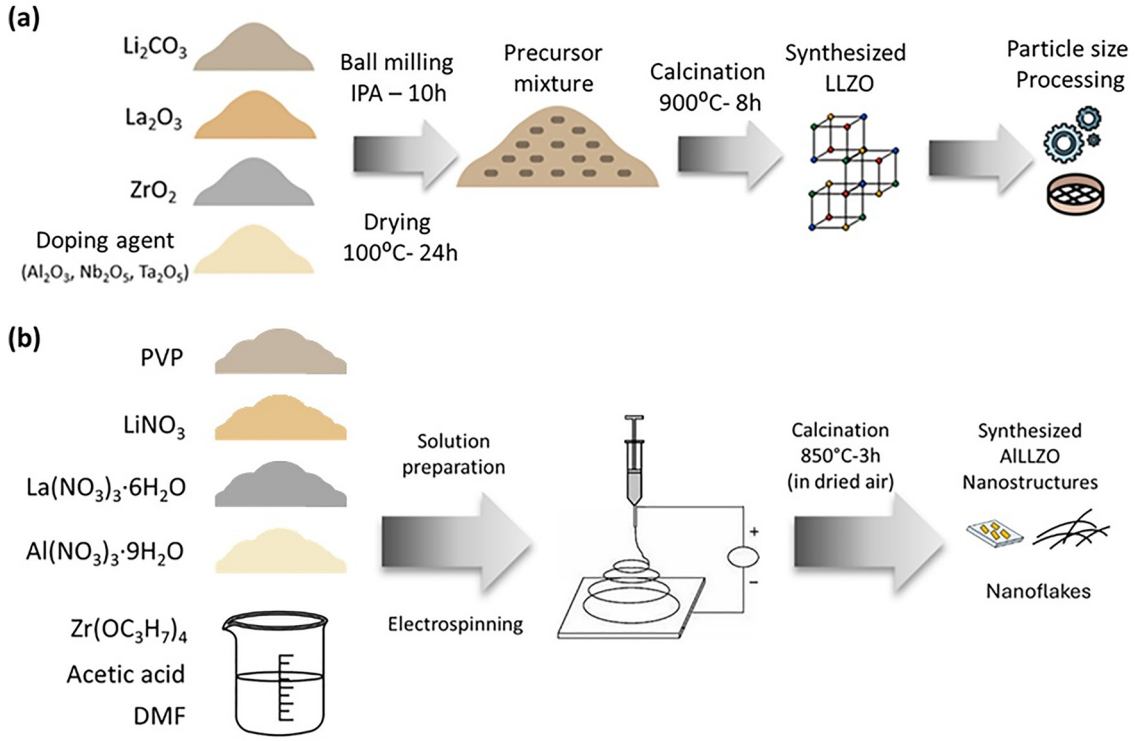

Fig. 1 Schematic representation of (a) solid-synthesis of Al and Ta/Nb LLZO particles and (b) synthesis of Al-doped LLZO particles by electrospinning.

(injector) and −17 to 23 kV (collector), a collector cylinder speed of 300 rpm, a needle to collector distance of 15–18 cm, six syringes with 23-stainless steel needles, a temperature of approx. 21 °C and a relative humidity of approx. 45%, and the entire process took approx. 6 h. Once the electrospinning process was completed under optimal conditions, the thermal treatment was performed in a furnace under a dry air flow of 10 L h^{-1} with a controlled heating rate of 0.5–5 °C min^{-1} up to 700–950 °C for 3–9 hours. After this step, the air atmosphere was replaced with argon to prevent the formation of Li_2CO_3. The synthesized Al-LLZO nanomaterials were then subjected to various physico-chemical characterization techniques. X-ray diffraction (XRD) was used to identify the crystalline phases, while high resolution scanning electron microscopy (HRSEM) provided insights into the morphology and size of the nanoflakes. Inductively coupled plasma mass spectrometry (ICP-MS) was employed to determine the metal elemental composition, while elemental analysis (EA) was conducted to detect any impurities present in the samples. A summary of the physical properties of the synthesized particles obtained through the different synthesis routes, including crystalline impurities and carbon content, is provided in Table S2.

PEO–LLZO electrolyte preparation. PEO–LLZO solid polymer electrolytes (SPEs) were prepared using LLZO as a ceramic filler. Three LLZO samples synthesized in this work were used as primary materials: S1, an Al-doped LLZO powder obtained *via* electrospinning; S2, a bulk Al-doped LLZO prepared by the solid-state reaction; and S3, a bulk Ta/Nb-doped LLZO also synthesized by the solid-state reaction. These materials were selected to evaluate the effect of dopant chemistry and the synthesis route on the performance of the resulting composite electrolyte. For comparison, a commercial LLZO powder (LLZO-1920M, Nanomyte, NEI Corporation, USA) was used as a reference material and is denoted as Ref. In all SPEs, 40 wt% LLZO particles were incorporated, as this loading provided the best balance of mechanical robustness and processability.

Poly(ethylene oxide) (PEO, $M_n \approx 600\,000$ g mol^{-1}) was purchased from Thermo Scientific, and LiTFSI (lithium bis(trifluoromethanesulfonyl)imide; Thermo Scientific, PO H27307) was used as the lithium salt. All solid materials were dried in a Büchi oven at 50 °C overnight prior to use. Anhydrous acetonitrile (ACN), employed as the solvent for SPE preparation, was purchased from Sigma-Aldrich. Electrolyte preparation was carried out inside a dry room with a dew point of −50 °C. Initially, 0.18 g of LiTFSI was dissolved in 23 g of ACN and sonicated for 60 seconds at room temperature (RT) using a Sonotrode S26d7. To this solution, 1.8 g of LLZO (40 wt%) was added, dispersed and sonicated for 300 s at RT, and further to this solution, 2 g of 600K PEO was added and stirred at RT overnight. Once the homogenised solution was formed, it was coated using a doctor blade on the siliconized PET substrate. The applicator gap for blade coating was set to 800 μm.

Finally, the SPE was dried at 60 °C overnight under vacuum in a Binder oven, then punched into 18 mm diameter disks (Fig. 2) and vacuum dried at 60 °C in a Büchi oven overnight. All dried samples and components were stored in an argon-filled glove box.

XRD

X-ray diffraction (XRD) measurements were conducted to evaluate the phase purity and crystal structure of the samples. The analysis was performed using a Malvern PANalytical X'Pert Pro

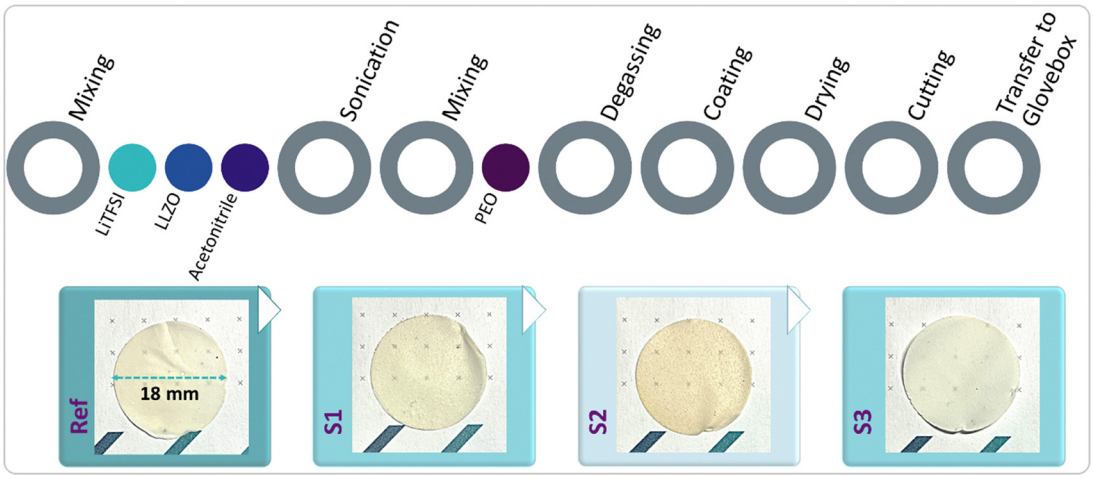

Fig. 2 Schematic representation of solid polymer electrolyte preparation.

MPD diffractometer (XRD Facility, Institut Català de Nanociència i Nanotecnologia), equipped with a Cu Kα radiation source (Kα = 1.54187 Å). Measurements were carried out at room temperature over a 2θ range of 10° to 60°, with increments of 0.05°.

ICP-MS

Inductively coupled plasma mass spectrometry (ICP-MS) analysis was performed using an Agilent 7500 Series ICP-MS instrument (Agilent Technologies, Santa Clara, CA, USA). Prior to measurement, the samples were weighed, digested in a 70% nitric acid (HNO_3) solution, and processed in an analytical microwave at 250 °C. After digestion, the residue was diluted for the analysis of the target elements.

SEM

SEM images were captured using a ZEISS Supra 40 electron microscope operated at an acceleration voltage of 3 kV. The samples were mounted on holders with silver paste in a dry environment to minimize exposure to ambient conditions during transfer to the microscope and were stored in a sealed container, which was opened only immediately before being placed into the instrument.

Ionic conductivity

The ionic conductivity was evaluated using electrochemical impedance spectroscopy (EIS) in a coin cell setup to maintain a consistent and uniform pressure across all samples. Measurements were conducted using a Biologic VMP-300 potentiostat. The frequency range spanned from 1 Hz to 1 MHz, with a signal amplitude of 10 mV. The electrochemical behaviour of the material was studied over a temperature range of 20 to 70 °C. Prior to each measurement, the samples were equilibrated at the target temperature for 1 hour to ensure thermal equilibrium. To extract key parameters, the Nyquist plots were fitted using Z View 3.0 software. Ionic conductivity was then calculated using the following equation:

$$\sigma = l/(R_b \times A)$$

where σ is the ionic conductivity (S cm^{-1}), l is the thickness (cm), A is the contact area (cm^2), and R_b (Ω) is the bulk resistance of the SPE membrane.

Voltammetry and chronoamperometry

The anodic stability of the SPE was evaluated using linear sweep voltammetry (LSV) up to 5.5 V *vs.* Li/Li^+. Additionally, cyclic voltammetry (CV) was performed at a scan rate of 50 mV s^{-1} to assess the electrochemical stability of the electrolytes using the Li‖SPE‖carbon coated Al cell configuration. Ion mobility and interfacial stability at the Li‖SPE interface were investigated through chronoamperometry in Li‖Li symmetric cells, applying a constant potential of 10 mV. All electrochemical measurements were conducted using a Biologic VMP-300 potentiostat.

Cell fabrication and cycling protocol

Li‖Li symmetric cells and Li–metal‖SPE‖NMC 811 full cells were prepared using CR2032 coin cell components. The cathodes were fabricated in-house by applying a slurry comprising $LiNbO_3$ coated NMC 811 (BASF), C65 (TIMCAL) and PVDF (SOLEF) in a weight ratio of 80 : 10 : 5 : 5 onto a carbon-coated aluminium current collector, using NMP as the solvent. The coated cathodes were dried at 120 °C under vacuum for 24 hours, followed by calendering to reduce their thickness by 15%, thereby increasing density and improving interparticle contact within the cathode structure. The calendered samples were then cut into 15 mm disks and assembled into lithium metal cells to evaluate their electrochemical performance in combination with the high energy density lithium metal anode.

For coin cell assembly, 16 mm diameter lithium disks were used, while NMC 811 cathodes with an active mass of 3 mg cm^{-2} were cut into 15 mm diameter disks (1.76 cm^2). Symmetric cell cycling was performed using a Biologic VMP-300 potentiostat while maintaining the cells in a climate chamber at 60.0 ± 0.1 °C. Li–metal‖NMC 811 full cells were cycled between 3.0 and 4.2 V at 60.0 ± 0.1 °C using a battery cycler Maccor 4000 series, with currents corresponding to C/10 for long-term cycling (Fig. 3).

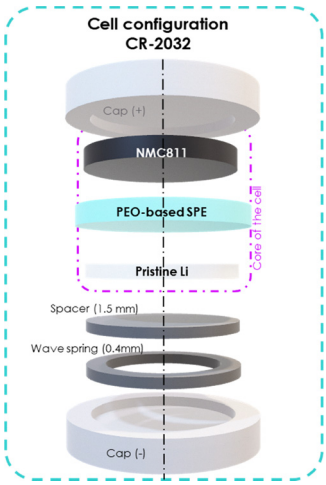

Fig. 3 Schematic representation of the coin cell configuration.

Results and discussion

Physicochemical characterisation

Fig. 4 presents the XRD diffraction patterns of the reference LLZO material with the sharp peaks at approximately 17°, 21°, 28°, 30.0°, 34°, 36°, 43°, 45° and 51–53° proving its cubic phase.[29] The low intensity peaks between 21 and 23° and at 30°, 47.5°, and 57° belong to impurities from Li_2CO_3 and $La_2Zr_2O_7$, respectively.[30] Fig. 4 also confirms that samples S1, S2 and S3 show a cubic LLZO garnet structure exhibiting major peaks similar to those of the Ref LLZO material with no significant peak splitting at 34–37° and 43–46°, ruling out the presence of tetragonal LLZO.[31] S1 shows minor impurities such as $La_2Zr_2O_7$ and Li_2CO_3 and appears to have uniform phase formation but still shows deviations in relative peak intensities compared to the Ref pattern, suggesting anisotropic grain alignment during synthesis.[32] Among the three samples, S2 is like Ref in both peak positions and relative intensities, indicating uniform phase formation.[33] S3 also matches the Ref well but with slight deviations and only traces of impurity phases are detected. The weak peaks near 21–22° in S2 correspond to Li_2CO_3, likely formed from the surface reaction with atmospheric CO_2, while the faint signal at 30.5°, 47.5° and 57° suggests minor $La_2Zr_2O_7$ residuals. These impurities are barely detectable in S3. The consistent sharp and narrow diffraction peaks across all samples and the Ref indicate high crystallinity, large grain size, and negligible microstrain. The excellent overlap in peak positions further confirms that no lattice distortion or compositional inhomogeneity is present within experimental resolution.[34]

ICP-MS and carbonate content

The stoichiometric ratios of all LLZO samples used in this study are reported based on experimentally measured ICP-MS elemental compositions: S1 contains Li (5.8 wt%), La (3.0 wt%), Zr (2.0 wt%) and Al (0.2 wt%); S2 contains Li (5.1 wt%), La (48.6 wt%), Zr (10 wt%) and Al (0.09 wt%); S3 contains Li (4.99 wt%), La (43.8 wt%), and Zr (17.6 wt%); and the commercial reference LLZO contains Li (6.28 wt%), La (3 wt%), Zr (2 wt%) and Al (0.24 wt%). These values represent the actual elemental composition of the materials and are used throughout the study when discussing their structural and electrochemical behaviour.

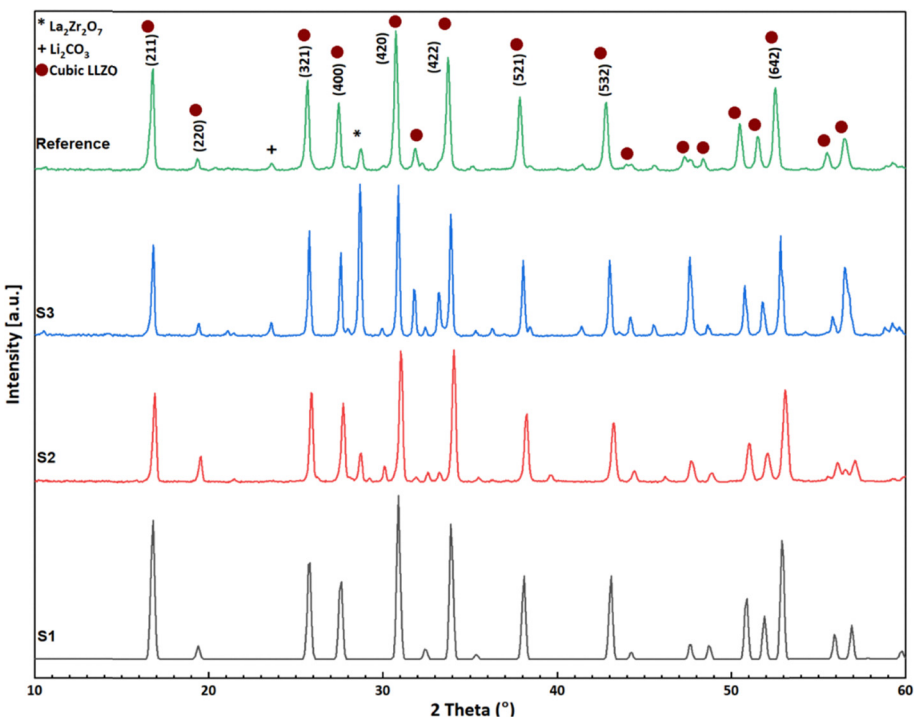

Fig. 4 XRD pattern of LLZO from different sources: S1 – Al-doped LLZO, synthesized *via* electrospinning (black); S2 – bulk Al-LLZO (red); S3 – bulk Ta/Nb-LLZO (blue) and Ref – commercial LLZO (green).

Table 1 ICP-MS analysis of the solid fillers from various sources

Element	S1% (w/w)	S2% (w/w)	S3% (w/w)	Ref% (w/w)
Li	5.8	5.1	4.99	6.28
Al	0.2	0.09	—	0.24
Zr	2	10	17.6	2
La	3	48.6	43.8	3
Nb	—	—	<0.01	—
Ta	—	—	<0.01	—

The ICP-MS analysis for S1 (Table 1) suggests a stoichiometry of $Li_{9.1}La_{3.1}Zr_2Al_{0.26}O_{17.8}$ *versus* a theoretical stochiometric $Li_{6.28}La_3Zr_2Al_{0.24}O_{12}$, evidencing a rather large formation of amorphous Li_2O_2 and other oxide species due to a considerable excess of Li (20 wt% excess) to avoid the loss of Li during thermal treatment and the fast cooling process. Kashif Khan *et al.* demonstrated that the formation of an exterior Li_2O_2 layer on LLZTO particles reduces crystallinity and improves Li-ion conductivity at the interface, thereby significantly enhancing the electrochemical performance of PEO-based composite electrolytes.[35]

The elemental analysis of the carbon (total carbon: elemental + organic + inorganic) (Table 2) was performed to determine the presence of Li_2CO_3, which is very usual to be present on the surface due to contact with air and passivates the material. A carbon content of S1, S2, and S3 samples is around 1.7, 0.82, and 1.35 wt%, respectively, suggesting the presence of various organic/inorganic carbonate compounds on the particle surface that could be possibly formed during synthesis and processing.

The surface characteristics of LLZO particles play a crucial role in governing their interaction with PEO, influencing the electrolyte's structural properties across different scales, as well as lithium-ion transport and interfacial stability. Surface degradation of LLZO not only results in the formation of LiOH and Li_2CO_3 layers but also facilitates Li^+/H^+ exchange, which can substantially affect lithium-ion dynamics, especially in proton-rich environments. As a result, LLZO with elevated surface carbon content is more likely to trigger unwanted parasitic reactions at the LLZO/PEO–LiTFSI interface and restrict ionic conductivity, ultimately compromising long-term electrochemical performance.[36]

Although ICP-MS shows that S2 (Zr ≈ 10 wt%) and S3 (Zr ≈ 17.6 wt%) deviate from the reference value (≈2 wt%), cubic LLZO phase formation is confirmed by XRD for all samples; thus, electrochemical comparisons are discussed in the context of the measured compositions and surface carbonate levels, rather than assumed nominal stoichiometry.

Table 2 Elemental analysis of elemental, organic, inorganic carbon and total carbon within the solid fillers

Sample	Sample weight (g)	TOC% w/w	EC% w/w	TIC% w/w	TC% w/w
S1	0.006	0.89	0.55	0.25	**1.70**
S2	0.066	0.53	0.16	0.12	**0.82**
S3	0.065	0.69	0.20	0.46	**1.35**

The obtained results are presented in % w/w of each type of carbon: TOC% w/w: g of total organic carbon per 100 g of sample. EC% w/w: g of elemental carbon per 100 g of sample. TIC% w/w: g of total inorganic carbon per 100 g of sample. TC% w/w: g of total carbon per 100 g of sample.

Morphology

To understand the morphology of LLZO particles, SEM analysis was performed, as shown in Fig. 5. S1 shows a flake like morphology after the thermal treatment, formed from a network of nanorods with an average length of approximately 385 nm, as demonstrated in Fig. S1, which is believed to enhance the ionic conductivity of the bulk LLZO material.[37] S2 shows the morphology of grains with various sizes, which, after sintering at 900 °C, have been reduced and arranged in a compact way, which may help in increasing the ionic conductivity of the electrolyte material and reduce the resistance of the battery. In S3, the doping of Nb/Ta resulted in the formation of larger particles due to the solid-state synthesis route.[38]

The interaction between the polymer matrix and inorganic fillers plays a crucial role in determining the mechanical, thermal, and ionic conductivity properties of PEO-based composite electrolytes, as well as their interfacial compatibility with lithium anodes and NMC cathodes. SEM is widely employed to evaluate the compatibility between different components of SPEs by identifying phase separations, pore formation, and surface roughness, which collectively influence interfacial stability.

The morphology and size of solid fillers also significantly affect the surface characteristics and overall structure of SPEs. Based on the literature, smaller and more uniformly distributed particles provide a larger polymer-filler interfacial area, which can facilitate Li^+ transport along the interfacial regions and improve interfacial exchange kinetics. In addition, oxide ceramic fillers may interact with lithium salts through Lewis acid–base interactions, promoting salt dissociation and increasing the concentration of mobile Li^+ ions. The polymer–ceramic interface can also generate space charge regions where ionic defect concentrations are modified, creating additional pathways for Li^+ migration. Furthermore, the presence of well-dispersed fillers can influence the segmental motion of PEO chains by reducing polymer crystallinity and increasing the amorphous fraction, which is known to enhance Li^+ mobility in PEO-based systems.[39–42] In this study, as shown in Fig. 6, the S1 based composite electrolyte exhibits a distinctly uneven surface, attributed to the relatively large LLZO particle size. In contrast, the Ref sample displays a smoother surface with a more homogeneous distribution of filler particles. On the other hand, the S2 and S3 based composite electrolytes, which possess a larger particle size in comparison to Ref, present a granular morphology. Additionally, some visible pores are observed within their structures, which is a common feature of PEO-based electrolytes prepared *via* solvent casting. These pores are primarily formed due to the rapid evaporation of acetonitrile during the fabrication process. Higher magnification surface images (Fig. S3) clearly demonstrate that samples S2 and S3 exhibit smoother surface features, which can potentially contribute to more uniform Li-ion exchange at the interface and enhance the efficiency of Li plating and stripping.

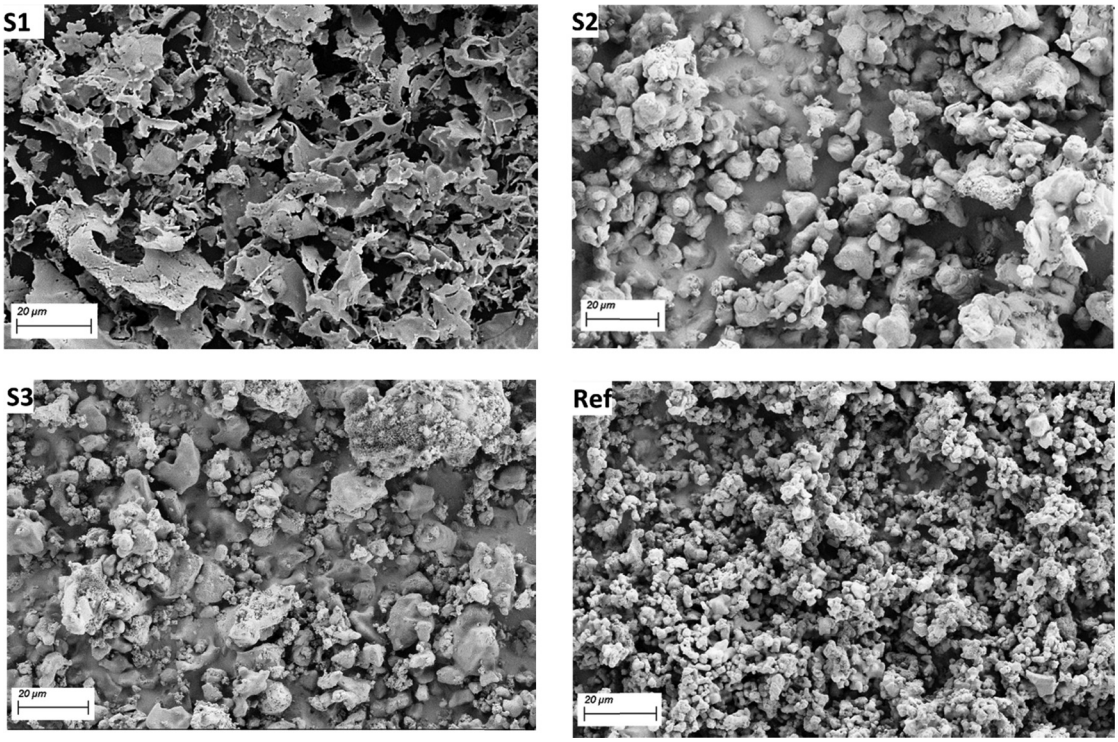

Fig. 5 SEM morphology of LLZO particles from different sources: S1 – Al-doped LLZO, synthesized *via* electrospinning; S2 – bulk Al-LLZO; S3 – bulk Ta/Nb-LLZO and Ref – commercial LLZO.

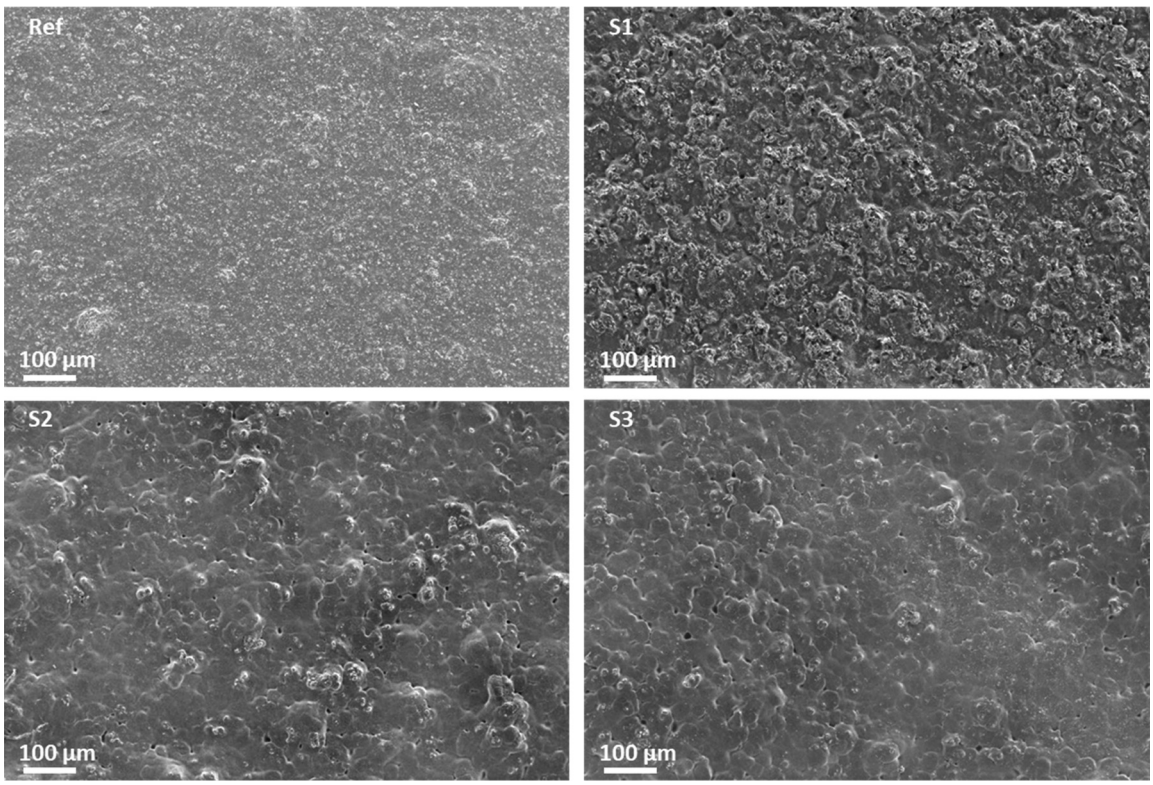

Fig. 6 Surface SEM micrographs of composite polymer electrolytes, each prepared from PEO (PEO : LiTFSI = 16 : 1) and containing 40 wt% LLZO filler particles. The composites differ only in the type of LLZO used: Ref – commercial LLZO, S1 – electrospun Al-doped LLZO, S2 – bulk Al-doped LLZO, and S3 – bulk Ta/Nb-doped LLZO.

Electrochemical characterisation

Ionic conductivity. The ionic conductivity of the PEO-based solid-state electrolyte with different LLZO samples is shown in Fig. 7. The S2 SPE exhibits the highest ionic conductivity for the entire temperature range even when compared to the Ref. The conductivity at RT is 10^{-4} S cm^{-1} and reaches up to 10^{-3} S cm^{-1} at 50 °C which is an acceptable value for state-of-the-art SPE electrolytes. The flake like morphology of the electrospun S1 LLZO leads to poor interparticle connectivity, thereby limiting the establishment of effective solid-solid contact. Non-uniform dispersion of the flakes within the PEO matrix, together with variations in interfacial contact, contributes to heterogeneous ionic pathways and restricts overall ionic transport. Nevertheless, the ionic conductivities of the various samples remain within a narrow range over the investigated temperature window; however, at lower temperature, the conductivity of all samples is primarily limited by segmental relaxation of the PEO chains, overshadowing differences introduced by the fillers.[43] The particle size and morphology of the solid fillers (Fig. 5 and Fig. S2) govern the degree of interparticle connectivity. The non-homogeneous particle size and uneven distribution lead to heterogeneous ion-transport pathways within the composite electrolyte, which directly influences the overall ionic conductivity. Moreover, the conductivity results can be correlated with the XRD, and S2 and the Ref sample show the cleanest cubic LLZO patterns with minimal impurities, which agrees with their higher ionic conductivity. In contrast, S1 and S3 exhibit slight deviations and minor impurity peaks, consistent with their lower conductivities due to reduced structural purity and increased resistance to Li^+ transport. In addition, the results achieved by ICP-MS and elemental analysis show that the S1 sample has more surface impurities across LLZO particles.[44]

Cyclic voltammetry, linear sweep voltammetry and constant voltage tests

SPEs possessing a broad electrochemical window are crucial for use in advanced Li battery technology especially when using high voltage cathodes. CV and LSV were performed at 60 °C for all these SPEs in Li‖CPE‖carbon coated Al current collector cells. Cycling voltammetry experiments were conducted to evaluate the kinetic reactions in the electrolyte, as shown in Fig. 8(a). All the electrolytes show stable performance in the wide voltage window of 2.5 to 4.5 V without the appearance of significant oxidation or reduction peaks. The S1 electrolyte shows a steep increase in oxidation peak at 4.5 V, whereas all the electrolytes are stable at rather high voltages and, thus, are expected to be stable with high voltage cathodes such as NMC 811.

LSV was performed to evaluate the electrochemical stability of the SPE within the voltage range of 1 V to 5.5 V, as shown in Fig. 8(b). Despite a small increase of current at ~2.9 V which may correspond to interfacial activation and initial ion/electron exchange, the main oxidation process, however, was triggered above 4.0 V across all samples. The Ref sample exhibited oxidation stability up to 4.5 V, while the S2 sample remains stable up to 4.25 V before a sharp rise in current was observed. In contrast, S1 and S3 showed an earlier onset of current increase, beginning at approximately 4.0 V. Such a behaviour in these SPEs may be attributed to the framework differences between PEO and LLZO components, which are likely influenced by the LLZO particle size and the morphology and

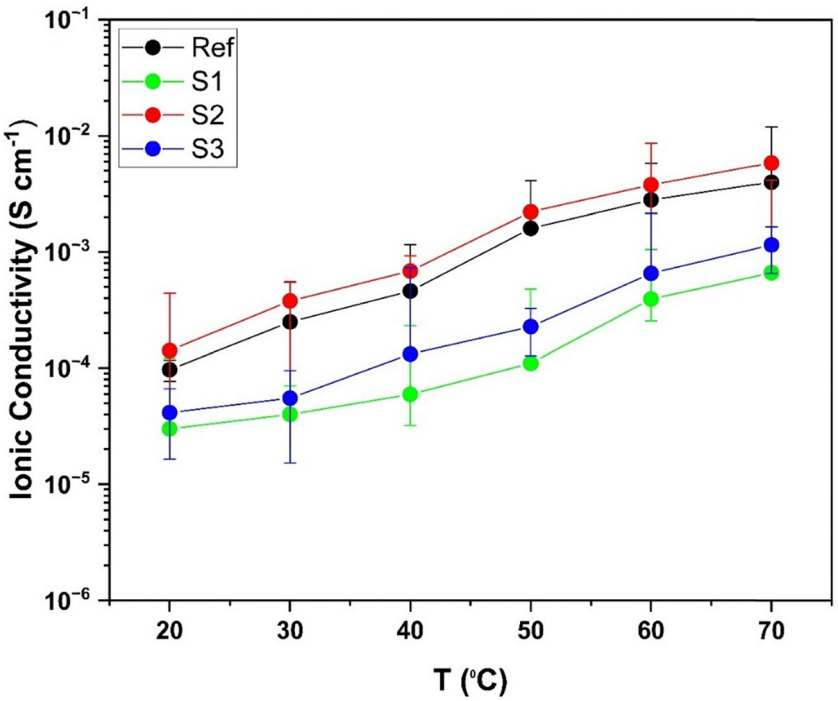

Fig. 7 Ionic conductivity of the PEO–LLZO based solid state electrolytes with a ±10% error bar from the instrument.

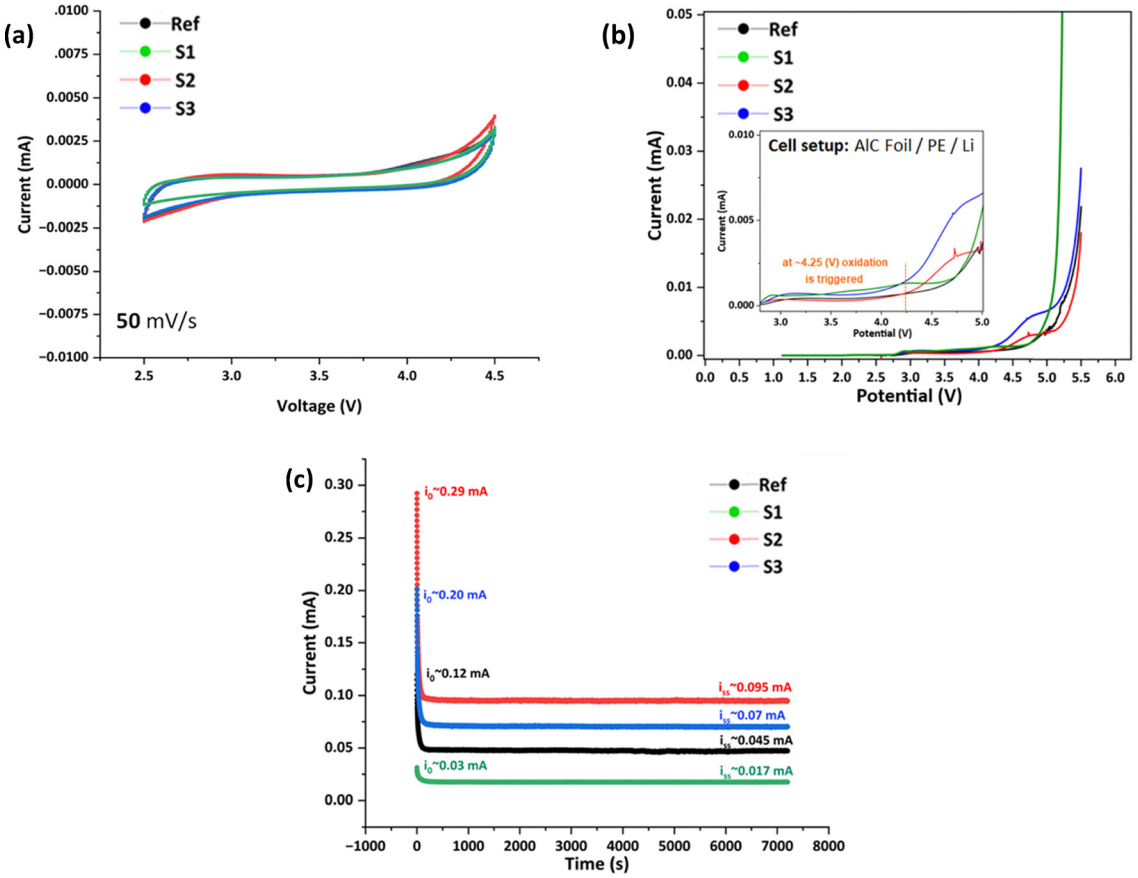

Fig. 8 (a) Cyclic voltammetry and (b) linear sweep voltammetry of Li‖SPE‖Al-C cells and (c) chronoamperometry of Li‖SPE‖Li cells with different LLZO-containing polymer electrolytes.

presence of impurities or inorganic by-products formed during synthesis and electrolyte fabrication. Such factors can significantly affect the high voltage oxidation potential and determine the onset of unwanted parasitic reactions.[24,45,46]

Beyond voltage stability, the ability to form a stable solid electrolyte interphase (SEI) that leads to preferable ion exchange at the interface is critical for extending the cycling lifespan. Therefore, chronoamperometry, performed using Li‖Li symmetric cells, is a valuable technique for assessing Li plating/stripping behaviour, the ion exchange rate and stability at the Li‖SPE interface. This method involves applying a constant potential and monitoring the current until it reaches a sustained steady-state phase. Fig. 8(c) presents the results of the chronoamperometry experiment applying a 10 mV constant potential. Among the tested samples, S2 exhibits the highest current in both the steady-state (I_{ss}) and triggering (I_0) phases, indicating lower interfacial resistance and enhanced charge transport, which contribute to improved ion mobility and interface stability. Conversely, samples S3, Ref, and S1 show lower I_0 and I_{ss} currents, still exhibiting a stable plateau with no signs of significant instability.

Symmetric cell cycling

To understand the lithium ion transport properties and lithium plating/stripping performance, Li‖SPE‖Li symmetrical cell cycling performance was evaluated at 60 °C with different current rates (0.01 mA, 0.02 mA, 0.03 mA, 0.05 mA, 0.1 mA and 0.2 mA) and a plating/stripping capacity of 0.05 mAh cm^{-2}. The polarization evolution was systematically studied throughout the process. The voltage response in these SPEs is shown in Fig. 9 at different current rates.

Beside the ion transport properties, cycling performance of the SPEs filled with LLZO particles in various sizes and morphologies is correlated with their structure at the interface with the lithium metal. While Fig. 6 shows various LLZO interface occupancies and Fig. 8(c) shows acceptable chronoamperometry stability, obtaining various overpotentials at an applied galvanostatic current (Fig. 9) suggests dependency of interface impedance with increasing LLZO occupied interface. Therefore, the Ref sample with a smaller LLZO particle size and homogenous particle distribution obtains the lowest overpotential at all applied currents. S2, S3 and S1 samples show increasing overpotentials due to embedded LLZO particles with a larger particle size, respectively. Besides obtaining higher overpotential, which suggests poor interface charge distribution and ion exchange and could cause poor long-term cycling performance, all samples demonstrate an arcing-type profile at all currents which indicates the diffusion-controlled process at the interface.[47] The Ref polymer electrolyte always shows the lowest overvoltage, possibly resulting in the optimised interface with the electrodes. However, in some cycles, it shows a second

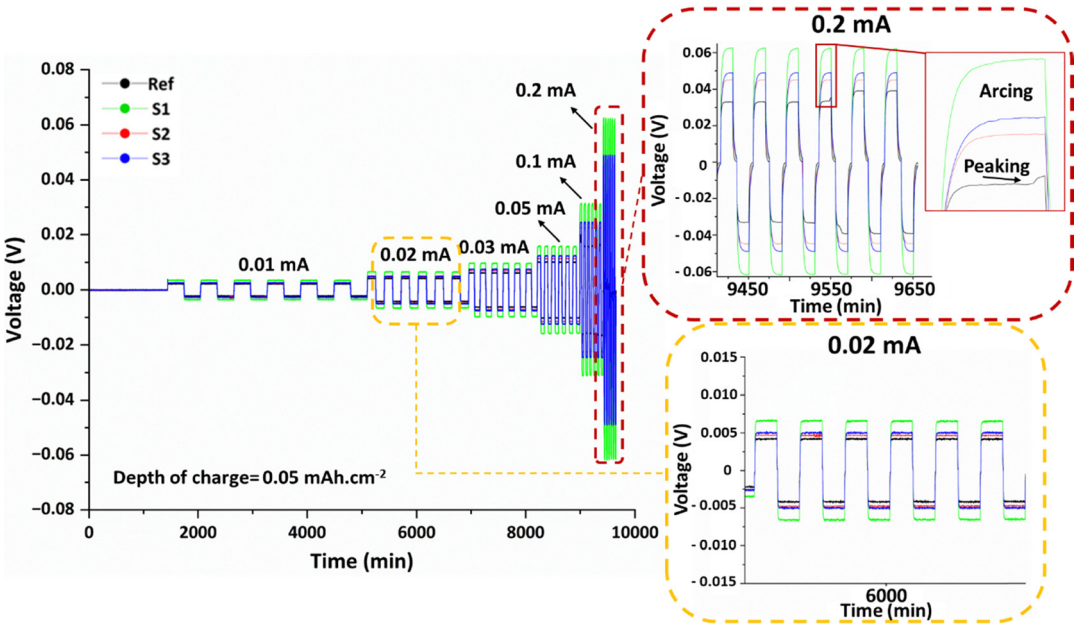

Fig. 9 Li‖Li symmetric galvanostatic cycling at C-rates and 0.05 mAh cm^{-2} plating/stripping cycling.

overvoltage step indicating a change in the charge transfer process, which could impact the lithium plating/stripping process and long-term cycling performance; however, further investigation is required to obtain a deeper and more conclusive understanding of this phenomenon.[48,49]

Full cell cycling

The voltage stability and long-term cycling performance were demonstrated with high voltage NMC 811 cathodes in the Li–metal full cell at 60 °C. The formation phase was performed using 2 cycles at C/30 up to a 4.2 V cut-off voltage. To evaluate the voltage stability of the SPEs with Li metal full cells, different voltage steps (3.9, 4, 4.1 and 4.2 V) were applied at C/10, as shown in Fig. 10. S2, S3 and Ref SPEs demonstrate their ability to reach up to 4.2 V with a discharge capacity of 80–115 mAh g^{-1}. While S2 is outperforming the rest, the S1 SPE shows the poorest performance overall, delivering a low discharge capacity of <50 mAh g^{-1} during the formation cycle. On the other hand, S2 and S3 show less discharge capacity fluctuation at a 4.2 cut-off voltage for long term cycling with 58% and 50% capacity retention at the end of cycling, respectively. Capacity fading of PEO electrolytes has already been investigated in multiple studies and is mostly attributed to formation of carbonyl groups and volatile degradation products such as 1,4-dioxane, and therefore capacity fading with the current PEO-based electrolyte when it is in contact with high voltage cathodes is inevitable.[49] Moreover, as

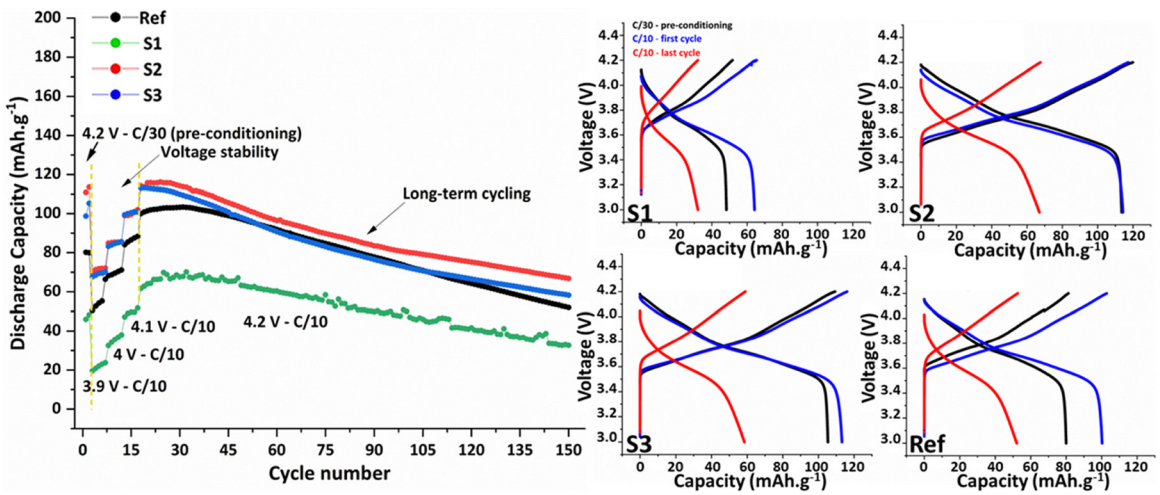

Fig. 10 Li metal full cell cycling of SPEs with the NMC 811 cathode and the Li–metal anode at 60 °C. Left side: Discharge capacity (mAh g^{-1}) *vs.* cycle number at different voltages: Ref (black), S1 (green), S2 (red), and S3 (blue). Right side: Voltage (V) *vs.* capacity (mAh g^{-1}) for C/30 pre-conditioning (black), C/10 in the first cycle (blue), and C/10 in the last cycle (red).

shown in Fig. 8b, the onset of oxidation occurs in the range of 4–4.25 V across the samples, which can trigger unwanted parasitic reactions and further aggravate discharge-capacity fading. Given that S1 has the highest surface carbon content (Table 2) and a flake-like morphology, exacerbated parasitic reactions at the cathode interface are a plausible contributing factor. In contrast, samples S2 and S3 exhibit higher ionic conductivity, a smoother surface morphology, and different dopant chemistries, all of which can potentially have a positive impact on their cycling performance. However, as it is demonstrated here, finding a suitable solid filler will improve not only mechanical integrity of the SPE but also the performance and lifespan of the cell.[50] The deviations from the ideal LLZO stoichiometry, together with the clear presence of Li_2CO_3 detected by ICP-MS and elemental analysis, are consistent with prior reports showing that LLZO readily forms LiOH and Li_2CO_3 surface layers upon exposure to air as in the case for S1, which significantly increase interfacial resistance, worsen Li wettability, and degrade electrochemical performance.[36]

Conclusions

Two different synthetic strategies, electrospinning and solid-state synthesis, have been developed to produce LLZO particles incorporating various dopants, including Al and Ta/Nb. XRD analysis of samples S1, S2, and S3 confirms the formation of the cubic garnet phase, as validated by the reference LLZO material. ICP-MS and elemental analysis reveal that sample S1 possesses the highest surface carbon content, whereas S2 exhibits the lowest.

A novel composite solid polymer electrolyte (SPE) was developed *via* solvent casting, comprising a PEO matrix, LiTFSI salt, and LLZO particles. The electrochemical performance of these SPEs was benchmarked against a reference SPE containing commercially available LLZO particles. Among the samples, SPE S2 exhibited significantly enhanced ionic conductivity ($\sim 10^{-3}$ S cm^{-1}) at 60 °C, compared to S1 and S3 ($\sim 10^{-4}$ S cm^{-1}), which is attributed to the compact grain arrangement observed in SEM. All SPEs demonstrated a wide electrochemical stability window ranging from 2.5 to 4.2 V, as confirmed by cyclic voltammetry and linear sweep voltammetry, further indicating that SPE S2 possesses superior electrochemical stability. Symmetric cell cycling at a current density of 0.5 mAh g^{-1} revealed that the reference sample, characterized by the smaller LLZO particle size and uniform distribution, achieved the lowest overpotential across all applied currents. In contrast, samples S1, S2, and S3 exhibited higher overpotentials due to the incorporation of larger LLZO particles. Full-cell cycling tests using the configuration NMC811‖SPE‖Li–metal at 60 °C showed that S2, S3, and the reference SPEs could operate up to 4.2 V, delivering discharge capacities in the range of 80–115 mAh g^{-1}. Sample S1, however, demonstrated inferior overall performance. The variation in surface carbon concentration is found to correlate with the ionic conductivity and electrochemical performance of the samples when employed in solid polymer electrolytes (SPEs). These findings underscore the critical role of LLZO particle characteristics such as the synthesis route, particle size, morphology, and dopant type in influencing the electrochemical behaviour of PEO based SPEs. The incorporation of LLZO fillers enhances interfacial stability in solid-state cell architectures, making the reported SPEs promising candidates for further optimization in lithium battery applications.

Author contributions

SSM contributed to analysing the data and writing the manuscript. SuM contributed to cell assembly, SEM analysis, and electrochemical characterisation. TS performed the SPE preparation. MH designed and executed the project. SMC and GP performed the synthesis and physical characterisation of electrospun LLZO. SP contributed to overall project guidance and revised the manuscript.

Conflicts of interest

There are no conflicts to declare.

Data availability

Supplementary information (SI) is available. See DOI: https://doi.org/10.1039/d5ya00355e.

The data supporting the findings of this study are available within the article. Additional raw data, including electrochemical measurements, characterization files, and analysis scripts, are available from the corresponding author upon reasonable request.

Acknowledgements

The authors would like to thank the European Commission (EC) and European Union/European Climate, Infrastructure and Environment Executive Agency (CINEA) for funding AM4BAT (grant no. 101069756) under Horizon-CL5-2021-D2-01-03.

References

1 J. Shaikh and B. Sharpe, *Assessment of light-duty electric vehicle costs in Canada in the 2023 to 2040 time frame*, International Council on Clean Transportation, 2023.
2 M. Armand, P. Axmann, D. Bresser, M. Copley, K. Edström, C. Ekberg, D. Guyomard, B. Lestriez, P. Novák and M. Petranikova, *J. Power Sources*, 2020, **479**, 228708.
3 X.-B. Cheng, R. Zhang, C.-Z. Zhao and Q. Zhang, *Chem. Rev.*, 2017, **117**(15), 10403–10473.
4 P. W. M. Jacobs, J. W. Lorimer, A. Russer and M. Wasiucionek, *J. Power Sources*, 1989, **26**(3–4), 503–510.
5 S. Lascaud, M. Perrier, A. Vallee, S. Besner, J. Prud'Homme and M. Armand, *Macromolecules*, 1994, **27**(25), 7469–7477.
6 S. M. Zahurak, M. L. Kaplan, E. A. Rietman, D. W. Murphy and R. J. Cava, *Macromolecules*, 1988, **21**(3), 654–660.

7 S. Toe, J.-C. Remigy, L. Leveau, F. Chauvet, Y. Kerdja and T. Tzedakis, *ECS Adv.*, 2023, **2**(4), 040509.
8 Z. Hu, H. Liu, H. Ruan, R. Hu, Y. Su and L. Zhang, *Ceram. Int.*, 2016, **42**(10), 12156–12160.
9 D. Bresser, S. Lyonnard, C. Iojoiu, L. Picard and S. Passerini, *Mol. Syst. Des. Eng.*, 2019, **4**(4), 779–792.
10 R. A. G. Whba, L. TianKhoon, M. S. Su'ait, M. Y. A. Rahman and A. Ahmad, *Arabian J. Chem.*, 2020, **13**(1), 3351–3361.
11 Q. Zhao, P. Chen, S. Li, X. Liu and L. A. Archer, *J. Mater. Chem. A*, 2019, **7**(13), 7823–7830.
12 N. A. Rahman, S. Abu Hanifah, N. N. Mobarak, M. S. Su'ait, A. Ahmad, L. K. Shyuan and L. T. Khoon, *PLoS One*, 2019, **14**(2), e0212066.
13 N. A. Aziz, S. R. Majid and A. K. Arof, *J. Non-Cryst. Solids*, 2012, **358**(12–13), 1581–1590.
14 M. H. A. Rahaman, M. U. Khandaker, Z. R. Khan, M. Z. Kufian, I. S. M. Noor and A. K. Arof, *Phys. Chem. Chem. Phys.*, 2014, **16**(23), 11527–11537.
15 N. Yazie, D. Worku, N. Gabbiye, A. Alemayehu, Z. Getahun and M. Dagnew, *Mater. Renewable Sustainable Energy*, 2023, **12**(2), 73–94.
16 Z. Du, X. C. Chen, R. Sahore, X. Wu, J. Li and N. J. Dudney, *J. Electrochem. Soc.*, 2021, **168**(5), 050549.
17 H. Wang, Q. Wang, X. Cao, Y. He, K. Wu, J. Yang, H. Zhou, W. Liu and X. Sun, *Adv. Mater.*, 2020, **32**(37), 2001259.
18 X. Zhang, T. Liu, S. Zhang, X. Huang, B. Xu, Y. Lin, B. Xu, L. Li, C.-W. Nan and Y. Shen, *J. Am. Chem. Soc.*, 2017, **139**(39), 13779–13785.
19 S. Liu, W. Liu, D. Ba, Y. Zhao, Y. Ye, Y. Li and J. Liu, *Adv. Mater.*, 2023, **35**(2), 2110423.
20 V. P. Hoang Huy, S. So and J. Hur, *Nanomaterials*, 2021, **11**(3), 614.
21 Y.-J. Wang, Y. Pan, L. Wang, M.-J. Pang and L. Chen, *Mater. Lett.*, 2005, **59**(24–25), 3021–3026.
22 Y. Li, T. Yang, W. Wu, Z. Cao, W. He, Y. Gao, J. Liu and G. Li, *Ionics*, 2018, **24**(11), 3305–3315.
23 J.-H. Choi, C.-H. Lee, J.-H. Yu, C.-H. Doh and S.-M. Lee, *J. Power Sources*, 2015, **274**, 458–463.
24 D. Cai, D. Wang, Y. Chen, S. Zhang, X. Wang, X. Xia and J. Tu, *Chem. Eng. J.*, 2020, **394**, 124993.
25 D. H. Kim, M. Y. Kim, S. H. Yang, H. M. Ryu, H. Y. Jung, H.-J. Ban, S.-J. Park, J. S. Lim and H.-S. Kim, *J. Ind. Eng. Chem.*, 2019, **71**, 445–451.
26 M. Li, W. Yang, L. Sun, Y. Li and X. Chen, *J. Energy Storage*, 2025, **118**, 116247.
27 H. L. Nguyen, V. T. Luu, M. C. Nguyen, S. H. Kim, Q. H. Nguyen, N. I. Nungu, Y. S. Jun and W. Ahn, *Adv. Funct. Mater.*, 2022, **32**(45), 2207874.
28 J. B. Kosctiuk, S. L. Reis, C. F. Gonin, F. E. Oliveira, R. L. Grosso, M. G. Franchetti, B. Leão, U. A. Stival, I. B. Gallo and L. M. Marquina, *Solid State Ionics*, 2024, **413**, 116607.
29 G. Larraz, A. Orera and M. Sanjuán, *J. Mater. Chem. A*, 2013, **1**(37), 11419–11428.
30 Ø. Gullbrekken, K. Eggestad, M. Tsoutsouva, B. A. Williamson, D. Rettenwander, M.-A. Einarsrud and S. M. Selbach, *Inorg. Chem.*, 2025, **64**(12), 5856–5865.
31 J. Awaka, N. Kijima, H. Hayakawa and J. Akimoto, *J. Solid State Chem.*, 2009, **182**(8), 2046–2052.
32 C. A. Geiger, E. Alekseev, B. Lazic, M. Fisch, T. Armbruster, R. Langner, M. Fechtelkord, N. Kim, T. Pettke and W. Weppner, *Inorg. Chem.*, 2011, **50**(3), 1089–1097.
33 R. Murugan, V. Thangadurai and W. Weppner, *Angew. Chem., Int. Ed.*, 2007, **46**(41), 7778.
34 Y.-J. Zhou, Y.-Q. Zhou, X.-Y. Li, H. Zhou, X. Huang and B. Tian, *Rare Met.*, 2025, 1–14.
35 K. Khan, H. Xin, B. Fu, M. B. Hanif, P. Li, B. A. Beshiwork, Z. Fang, M. Motola, Z. Xu and M. Wu, *J. Colloid Interface Sci.*, 2023, **642**, 246–254.
36 P. Ghorbanzade, P. López-Aranguren and J. M. López del Amo, *ChemElectroChem*, 2024, **11**(11), e202400136.
37 Q. H. Nguyen, V. T. Luu, H. L. Nguyen, Y.-W. Lee, Y. Cho, S. Y. Kim, Y.-S. Jun and W. Ahn, *Front. Chem.*, 2021, **8**, 619832.
38 J. Xue, K. Zhang, D. Chen, J. Zeng and B. Luo, *Mater. Res. Express*, 2020, **7**(2), 025518.
39 F. Croce, L. Persi, B. Scrosati, F. Serraino-Fiory, E. Plichta and M. J. E. A. Hendrickson, *Electrochim. Acta*, 2001, **46**(16), 2457–2461.
40 B. Scrosati, F. Croce and L. Persi, *J. Electrochem. Soc.*, 2000, **147**(5), 1718–1721.
41 D. Zhang, X. Meng, W. Hou, W. Hu, J. Mo, T. Yang, W. Zhang, Q. Fan, L. Liu and B. Jiang, *Nano Res. Energy*, 2023, **2**(2), e9120050.
42 D. Zhou, D. Shanmukaraj, A. Tkacheva, M. Armand and G. Wang, *Chem*, 2019, **5**(9), 2326–2352.
43 M. Keller, G. B. Appetecchi, G.-T. Kim, V. Sharova, M. Schneider, J. Schuhmacher, A. Roters and S. Passerini, *J. Power Sources*, 2017, **353**, 287–297.
44 K. Parascos, J. L. Watts, J. A. Alarco, Y. Chen and P. C. Talbot, *RSC Adv.*, 2022, **12**(36), 23466–23480.
45 H. Zhang, M. Klimpel, K. Wieczerzak, R. Dubey, F. Okur, J. Michler, L. P. H. Jeurgens, D. Chernyshov, W. van Beek and K. V. Kravchyk, *Chem. Mater.*, 2024, **36**(22), 11254–11263.
46 S. Vema, F. N. Sayed, S. Nagendran, B. Karagoz, C. Sternemann, M. Paulus, G. Held and C. P. Grey, *ACS Energy Lett.*, 2023, **8**(8), 3476–3484.
47 D. Rakov, M. Hasanpoor, A. Baskin, J. W. Lawson, F. Chen, P. V. Cherepanov, A. N. Simonov, P. C. Howlett and M. Forsyth, *Chem. Mater.*, 2021, **34**(1), 165–177.
48 G. Rollo-Walker, M. Hasanpoor, N. Malic, F. M. Azad, L. O'Dell, J. White, J. Chiefari and M. Forsyth, *Phys. Chem. Chem. Phys.*, 2024, **26**(21), 15742–15750.
49 Q. Lv, Y. Jing, B. Wang, B. Wu, S. Wang, C. Li, L. Wang, L. Xiao, D. Wang and H. Liu, *Energy Storage Mater.*, 2024, **65**, 103122.
50 H. Zhang, J. Zhang, J. Ma, G. Xu, T. Dong and G. Cui, *Electrochem. Energy Rev.*, 2019, **2**(1), 128–148.